Geometry Effects on Joint Strength and Failure Modes of Hybrid Aluminum-Composite Countersunk bolted Joints

Calin Dumitru Coman
National Institute of Aerospace Research (INCAS) "Elie Carafoli", Romania
coman.calin@incas.ro

Daniel Eugeniu Crunteanu
Faculty of Aerospace Engineering, Polytechnic University of Bucharest, Romania
daniel.crunteanu@upb.ro

Grigore Cican
Faculty of Aerospace Engineering, Polytechnic University of Bucharest, Romania
grigore.cican@upb.ro (corresponding author)

Marius Stoia-Djeska
Faculty of Aerospace Engineering, Polytechnic University of Bucharest, Romania
marius.stoia@upb.ro

Received: 4 October 2023 | Revised: 25 October 2023 | Accepted: 2 November 2023

 DOI: https://doi.org/10.48084/etasr.6472

ABSTRACT

This paper presents the effects of geometry parameters (width/hole diameter, and edge distance/hole diameter ratios) on the damage initiation and growth in the CFRP (Carbon Fiber Reinforced Polymer) composite-aluminum countersunk bolted joints. Strain gauge measurements conducted with an Instron testing machine along with a detailed 3D finite element model incorporating geometric, material, and friction-based contact nonlinearities were used to investigate the geometry parameters on the Progressive Damage Analysis (PDA) of the orthotropic material model. The PDA material model integrates the lamina nonlinear shear deformation, Hashin-type failure criteria, and strain-based continuum degradation rules, using the UMAT user subroutine in the MSC Software Corporation Patran-Nastran commercial software. The results showed that the geometry effects on damage initiation and failure modes are quite accurately predicted by the PDA material model, which proved to be computationally efficient, and therefore can predict failure propagation and damage mechanisms. Plate geometry is an important parameter in the design process of an adequate bolted joint while its effects on damage initiation and failure modes were quite accurately predicted by the analysis. The latter proved to be computationally efficient, and could successfully predict failure propagation and damage mechanism in hybrid metal-composite countersunk bolted joints.

Keywords-progressive damage; failure mode; strength

I. INTRODUCTION

The aerospace industry became the most common application field for fiber reinforced Polymer Matrix Composites (PMCs) due to their lightweight properties [1]. These structural components are often assembled in conjunction with metal parts, using mechanically fastened joints, resulting in hybrid metal-composite joints, which generate some challenging problems for mechanical engineers. Poorly designed hybrid joints not only are a source of failure, but could also lead to a reduction of the whole structure durability and reliability. Researchers commonly study failure analysis of composite bolted joints, using a method that combines Continuum Damage Mechanics (CDM) [2] with Finite Element Analysis (FEA). In the CDM case, the local damage onset appears at low values of the applied load. Damage accumulation is developed with increasing load according to damage propagation laws, which makes the method accurate, and able to predict various failure modes. The major disadvantage of the CDM models is the huge amount of test data required for model calibration.

Progressive Damage Analysis (PDA) of composite materials, which is based on the stress-strain failure criterion [3], showed that the material orthotropic property reduction due to damage initiation is essential for stress field analysis [4-7]. Intralaminar damage initiation based on the local stress-strain state and the subsequent stiffness degradation that reflects damage were primarily investigated within the framework of CDM. On the contrary, delamination and, to a limited extent, matrix cracking were studied with the help of interface fracture mechanics approaches as cohesive zone models and virtual crack closure techniques. Combining both approaches for the PDA of PMCs is an analysis procedure employed for laminate failure. Matrix microcracking may lead to a split as a localized phenomenon, and then a mesomodel approach [8] can be used. A Discrete Ply Model (DPM) along with cohesive elements placed at the interfaces between solid elements to represent matrix cracks and delamination allow the natural coupling between the intra- and inter-laminar damage to be naturally taken into account. The former can be utilized for a computational study of scaled open-hole tensile tests [9], or for the failure mode called pull-through to test fasteners in laminates [10] where the splitting and load redistribution effects were correctly predicted. Many PDA models [11-15] incorporate shear nonlinearity, the Hashin type failure criterion and constant elastic property degradation laws for orthotropic materials. These make the method quite easy to implement and computationally efficient. Since these property degradation models use constant factors for the elastic property reduction due to damage growth, they cannot predict the bearing final failure. A design methodology for mechanical fastened joints in composite laminates was proposed in [11] to forecast the final failure and failure modes by using point or average stress models. A comprehensive review on the available degradation models for PDA, containing 310 references, was organized in [16] around the relationships of the various models together with the frameworks employed for finite element implementation. A continuum based progressive damage model for fiber-reinforced composites, implemented in ABAQUS, considered two failure modes: catastrophic net-section tension-failure and non-catastrophic accumulation of bearing damage [17]. Models containing continuous degradation rules intending to improve the numeric algorithm convergence, and to obtain a smoother load-displacement curve have started to appear in literature [18, 19]. One major deficiency of these models is that they focus only on a few types of failure modes, and do not consider the various joint failure modes. The composite progressive damage behavior is a complex nonlinear phenomenon, and in conjunction with geometric and contact nonlinearities can lead to convergence loss in the Finite Element Method (FEM) analysis. This mostly occurs in implicit numerical algorithms, which imply that many efforts are made for obtaining a valid solution towards predicting the ultimate global structure failure. Composite materials can withstand an increased temperature up to 300 ^{o}C, having favorable properties such as high pressure resistance, low thermal expansion coefficient, high thermal conductivity, high thermal shock resistance, and low depression [20, 21]. The difficulties arising from composite material usage on structural failure problems are that these materials have anisotropic mechanical properties, brittle behavior, and low interlaminar strength [22]. Another issue is the damage variation with temperature [23-26]. Also, various structures can be exposed to rush environment conditions that may cause joint strength loss because of environmental aging and temperature variations [27-31].

In this paper, a progressive damage analysis using an adequate material model for a hybrid metal-composite countersunk single bolted joint is described and developed. The numerical model can predict the geometrical parameter (width/hole diameter and edge distance/hole diameter ratios) effects on the structural behavior and failure modes. It takes into account all the nonlinearity phenomena involved in the load transfer through the joint, i.e. geometric nonlinearity (large deformations), friction based full nonlinear contact, and material nonlinearities due to the lamina shear deformations. Hashin-type failure and strain-based continuous degradation model were implemented using a user defined subroutine in the commercial software MSC Nastran SOL 400 solver. A series of standard bearing tests were conducted in the laboratory to validate the three-dimensional finite element model and PDA results. The influence of geometrical parameters on the failure modes of the countersunk hybrid metal-composite joints is a task relevant to the aeronautic field of engineering and maintenance for structural applications. An example is the attachment bolts of the visiting covers on the exterior skin of airplane wings. The experimental and numerical results fit quite accurately capturing the impact of geometrical parameters on stiffness, failure load, and failure modes.

II. MATERIALS AND METHODS

A. Joint Geometry

Single-Lap Joints (SLJs) with countersunk bolts were manufactured using metal and composite materials for the adherents. Joint geometry is presented in Figure 1. The joint design was chosen in accordance with ASTM D 5961 [32] to induce bearing failure. The in-plane dimensions of each plate are illustrated in Table I and Figure 1.

TABLE I. EXPERIMENT SET-UP

Case	No. of specimens	Length (mm)	Width (mm)	Edge distance (mm)	*e/D* (-)	*b/D* (-)	Bolt torque (Nm)
1	5	150	34	10	2.5	6.8	0.5
2	5	150	42	15	3.75	8.4	0.5
3	5	150	50	20	5	10	0.5

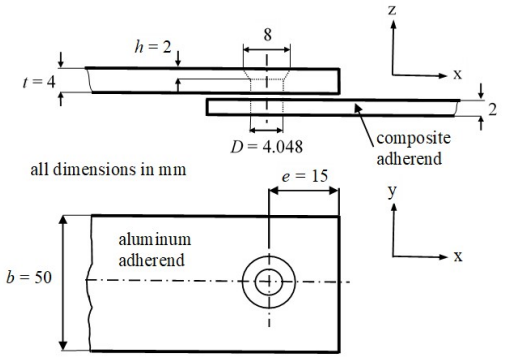

Fig. 1. Countersunk hybrid joint geometry.

Material thicknesses are different, 4 mm for the metal plate and 2 mm for the laminated plate. Countersunk head stainless steel bolts with nominal diameter of 4 mm were used. The applied torque level for the bolt is 0.5 N·m. A similar geometry was utilized in [33]. Special attention is given to the conditions for obtaining bearing failure as: $b/D > 4$, $e/D > 3$, $1.5 \leq D/t \leq 3$, $0 \leq h/t \leq 0.7$ (Figure 1). The shank of the bolt does not bear the hole surface due to the initial clearance in the joint. The joint under investigation has a close tolerance clearance equal to 48 μm according to f7H10 [34]. The hole has therefore a diameter $D = 4.048$ mm.

B. Materials and Specimen Manufacturing

Countersunk head stainless steel bolts in dry conditions were considered. The composite adherent was manufactured from carbon-epoxy pre-preg layers with 32% fiber volume fraction by SC AVI SRL Craiova Dolj. The stacking sequence of the composite laminate adherent is represented by [0/90/0/90/0/90], using 0.33 mm thickness unidirectional lamina with the elastic properties presented in Table II. The aluminum adherent was manufactured from AA 7075T6 aluminum alloy [40] by AMARI Metal Innovations. The standard bolts, nuts, and washers were fabricated from stainless steel A2-70 [40] with the elastic properties presented in Table III. The presented (Table II) lamina elastic properties were obtained experimentally following the ASTM standards [35-37] by performing tests on the unidirectional laminated specimens. The constitutive behavior of the composite material was considered linear for traction and compression and nonlinear for shearing based on the experimental results. The latter were obtained after testing specimens with unidirectional fibers, longitudinal and perpendicular to the fiber direction. Shear deformation was acquired using the Iosipescu test on notched specimens and traction for specimens cut at 45º with respect to the alignment of 0/90º to get fibers at 45º. The lamina orthotropic directions (1, 2, 3) are the same with the global coordinate axes (x, y, z) shown in Figure 1. Regarding the Coefficient of Thermal Expansion (CTE) of the composite adherent, the micro-analysis method was used to calculate it at lamina level utilizing the coefficients of thermal expansion of fibers and matrix. According to [38, 39] we considered $\alpha_{fiber} = -0.41.10^{-6}$ /ºC and $\alpha_{matrix} = 40 .10^{-6}$ /ºC. With these values, it can be obtained [3]:

$$\alpha_{11} = \frac{E_{fiber} \cdot V_{fiber} \cdot \alpha_{fiber} + E_{matrix} \cdot (1 - V_{fiber}) \cdot \alpha_{matrix}}{E_{11}} = 2 \cdot 10^{-6} \text{ /°C}$$

The thermal expansion coefficients on the other two directions are $\alpha_{22} = \alpha_{33} = 44^{-6}$/°C. For the metallic parts of the joint, the material properties were taken from [40].

C. Joint Geometry

SLJs were prepared to study the influence of geometry parameters (width/hole diameter and edge distance/hole diameter ratios) on the failure mechanisms in the laminated adherent. There were no compensation tabs used to align the joint in the grips, considering that this boundary condition is closer to reality in practical applications. Therefore, it was expected to acquire bending effects in the adherents, most of which in the composite ones. After joint mounting, the specimens were gripped in the 30 kN Instron 3367 testing machine, and were connected to a temperature-controlled chamber [41]. The chamber is Instron SFL 3119-400, temperature-controlled (-70/+250 ^{o}C) with liquid CO_2 as freezing agent. The bearing tests were conducted in accordance with ASTM 5961 [32], and the specimens were loaded with a displacement rate of 0.3 mm/min until ultimate failure, in temperature $T = +50$ ^{o}C. A voltage generator and an oscilloscope were used for Structural Health Monitoring (SHM) with Lamb waves.

TABLE II. COMPOSITE MATERIAL PROPERTIES

Property	Carbon fibers [38]	Epoxy matrix [39]	Lamina Exp.
Longitudinal modulus E_{11} (MPa)	230000	3200	34433
Transversal modulus E_{22} (MPa)	6000	3200	3610
Through-thickness modulus E_{33} (MPa)	-	3200	3610
Shear modulus G_{12} (MPa)	18000	1300	2421
Shear modulus G_{23} (MPa)	-	1300	2421
Shear modulus G_{13} (MPa)	-	1300	1561
Poisson coefficient ν_{12}	0.36	0.35	0.36
Poisson coefficient ν_{23}		0.35	0.45
Poisson coefficient ν_{13}		0.35	0.35
Longitudinal CTE α (10^{-6}/ºC)	-0.04	4	2
Transversal CTE α (10^{-6}/ºC)	-	-	44
Through-thickness CTE α (10^{-6}/ºC)	-	-	44
Longitudinal tensile strength $\sigma_{11\,max}^{T}$ (MPa)	3530	86	253
Longitudinal compression strength $\sigma_{11\,max}^{C}$ (MPa)	-	-	230
Transversal compression strength $\sigma_{22\,max}^{C}$ (MPa)	-	-	74
In plane shear strength τ_{12}^{max} (MPa)	-	-	25
Out plane shear strength τ_{23}^{max} (MPa)	-	-	37
Out plane shear strength τ_{13}^{max} (MPa)	-	-	37

TABLE III. ISOTROPIC MATERIAL PROPERTIES OF THE METALLIC PARTS [40]

Property	AA 7075T6	A2-70
Elastic modulus E (MPa)	71016	206000
Shear modulus G (MPa)	26890	75842
Poisson coefficient ν	0.33	0.36
Thermal coefficient CTE α (10^{-6}/ºC)	24	18

III. RESULTS AND DISCUSSION

A. Finite Element Model

A three-dimensional (3D) FEM model, using linear brick 8-node elements, was developed in MSC Nastran for the joint geometry model, as it is shown in Figure 2(a). Each separate part was modeled: aluminum and composite adherents, the washer, and a combined bolt-nut part. The adherents were modeled with in-creased radial mesh density around the hole where high strain gradients exist. Regarding the joint clamping in the testing machine, the boundary conditions imposed on the FE model are presented in Figure 2(a). The displacements u, v, and w are defined along the x, y, and z directions. The boundary conditions represent clamping of the nodes on top and bottom surfaces at the end of the aluminum adherent. They additionally block the translations on y and z directions (v and w) at the rightmost end of the composite adherent. This is only

observed, though, on the surface of the adherent over the length of 70 mm. Each side was griped during the test to agree with the experiment. The other nodes through the thickness of the lap joint were not blocked in the experimental test or in the simulation. The tabs at the end of the adherents were considered to reciprocally compensate their thickness when gripped. The intention was to induce bending as it may often happen in practice. For simulating the quasi-static loading condition of the testing machine, a prescribed u displacement on the x direction was applied to the nodes from both surfaces of the composite adherent at the rightmost end.

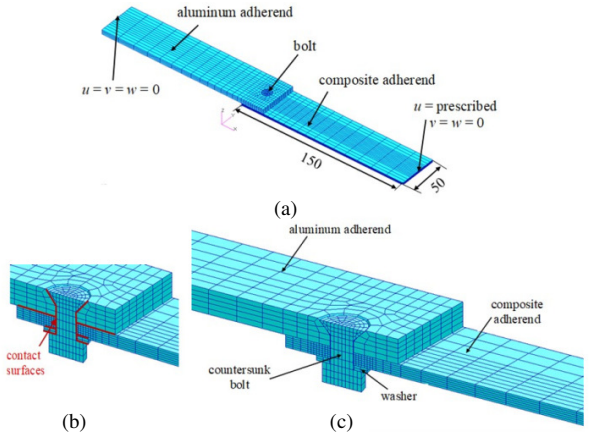

Fig. 2. 3D finite element model: (a) hybrid joint with boundary conditions, (b) contact surfaces marked with red color, (c) countersunk bolt joint assembly.

In order to avoid rigid body motions in FEA analysis, light springs were attached to the not fully constrained components such as the bolt, the washer, and the laminated adherent. For simulating the bolt pre-load due to the applied torque level, a 330 N axial force was applied in the bolt shank, using the pretension section from the Bolt Preload Module of MSC Patran-Nastran. The composite laminated adherent is modeled with continuum solid-shell advanced elements available in MSC Patran-Nastran. These special solid elements have bending properties like shells and one integrating point per element is considered. The finite element model has 6 elements across the laminate thickness, with one solid-shell element per each ply, thus, stress in each ply can be determined and the correct bending-twisting coupling is obtained. The number of elements and nodes for each part of the finite element model is given in Table IV.

TABLE IV. FEM MODEL DESCRIPTION

Part	Elements	Nodes
Composite adherent	3568	3284
Metal adherent	2413	2318
Bolt	862	824
Washer	394	357
Total	7237	6783

In the 3D model, the contact with clearance between the bolt and the surface of the hole is realized as follows. The method requires the definition of the bodies that can come into contact. The contact bodies may be the whole physical bodies (laminated adherents, bolt, washer). However, it has been shown in [42] that it is more efficient to consider element sets of these physical bodies, as shown in Figure 2(b), because the number of checks for contact between bodies at each iteration of the solution is reduced. The finite element model was refined in the vicinity of the hole so as to better capture the effects of stress concentrators (Figure 2(c)). Therefore, the minimum element length is 0.33 mm around the hole. The minimum element length is increasing from hole towards the clamped ends of the adherents. Another step in defining nonlinear contact phenomena is the choice between the discrete contact and the analytical contact. When a node on a solid reaches the contact segment on the other contact body, the node is constraint on this segment with respect to the normal of this segment. In the case of discrete contact for normal detection, the linear representation with the finite elements of the contact surface is used, which leads to the calculation of each element normal. If the surface is not planar, then when a node touches the contact segment it is blocked between two different normal elements due to their discontinuity, and is shifted and constrained on the contact segment. This impediment has an adverse effect on the quality [42]. In the case of analytical contact, a smooth Coons surface is constructed through the nodes of the solid contact segment. Later, this analytical surface is used to calculate the normal of the contact surface between the two solids, thus solving the problem of node blocking due to the discontinuity of the surface normal between the bodies. This method leads to a better representation of the joint geometry. Especially, its deformation and the accuracy of the numerical results are far superior to those of the discrete contact technique. Consequently, the former method was applied in this work.

B. Model Validation

In this section, the results generated from the tests are compared with the ones of the 3D FEM. Strains in the selected points on the surface of the laminated adherent were used to check the model accuracy. On the composite adherent, strain gauges were applied, and the joint was loaded in tension to a level that prevents any important damage of the composite adherent (1.2 kN load) at T_1 = +50 ^{o}C. Figure 3 depicts the locations of the 3 mm length strain gauges, type 1-Ly16-3/350, with 350 Ω electrical resistance, fabricated by HBM. Gauges 1, 3, and 4 were aligned with the loading direction and were located on the bottom surface of the laminate adherent, except gauge number 2. This was located in the shear plane on the composite adherent top surface in the same location but opposite to gauge number 1. The numerically calculated and experimentally measured strains are given in Table V and Figure 4. The notations in Figure 4 are: Exp. curves denote the variation of experimentally acquired strains and FEM the numerical ones. From Table V, it is clearly shown that strain gauges 1 and 2 indicate a joint bending, although the loading is a tensile one. The strain readings for gauges 3 and 4 are somehow different, indicating a misalignment effect of the joint along the longitudinal axis, which is the loading x axis. As a conclusion, it can be considered that the model has quite satisfactorily predicted the joint linear behavior, and can be further used in temperature parametric studies for the linear response of the hybrid aluminum-composite joint.

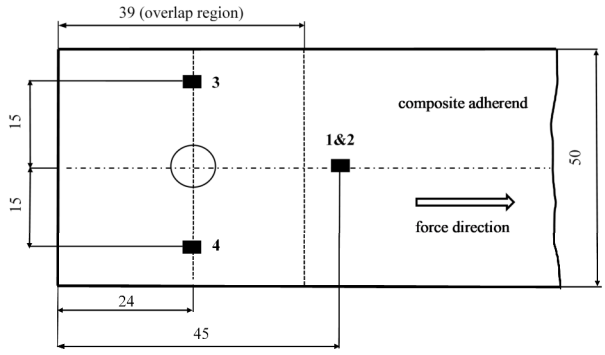

Fig. 3. Strain gauge locations, all dimensions in mm.

TABLE V. EXPERIMENTAL AND NUMERICAL STRAIN READINGS FOR 1.2 KN APPLIED LOAD

Gauge number	Experimental (Exp.) strain (μm/m)	Numerical (FEM) strain (μm/m)
1	776	810
2	-1300	-1252
3	757	689
4	679	615

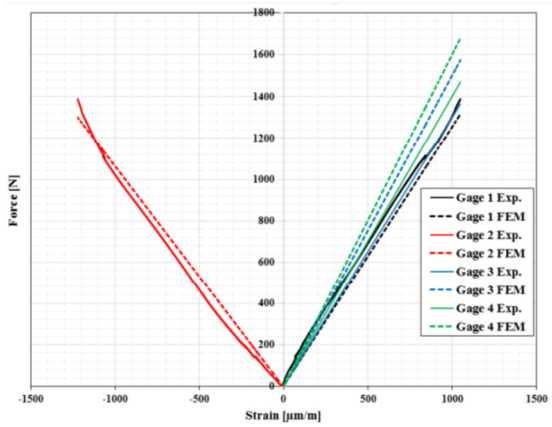

Fig. 4. Experimental and numerical surface strains.

The results of the acoustic simulations highlighted once more that the position of the resonators influences both the acting frequency of the resonators and their effectiveness, leading to a reduction of the attenuation (Figure 8).

C. Nonlinear Shear Deformation

In order to take into account the nonlinear behavior of the composite adherent within the hybrid metal-composite joint, the simulation must account for the two most important nonlinear mechanisms: lamina nonlinear shear deformations and stiffness reduction due to damage accumulation at the lamina level. These two nonlinearities are considered by using an external user-defined subroutine named User_mat, edited in FORTRAN. User_mat calls the modified predefined MSC Nastran subroutine UMAT in order to implement the material nonlinearities specified above. Authors in [44] developed the in plane nonlinear shear stress-strain constitutive model at the lamina level, utilizing the high order elasticity theory.

D. Failure Criteria and Continuous Degradation Rules

The most dominant micro-failure modes for bearing joints are matrix compression, fiber compression and fiber-matrix shear modes. In [45], failure criteria for unidirectional laminates are used in the PDA of the laminated adherent around the hole, as the failure indexes are calculated with relation (1) for matrix compression and (2) for fibers compression-shear damages:

$$\mathrm{FI}_1 = \left[\left(\frac{\sigma_{22,\max}^{C}}{2\tau_{23}^{\max}}\right) - 1\right]\frac{\sigma_2+\sigma_3}{\sigma_{22,\max}^{C}} + \frac{(\sigma_2+\sigma_3)^2}{4(\tau_{23}^{\max})^2} - \frac{\sigma_2\cdot\sigma_3}{(\tau_{23}^{\max})^2} + \left(\frac{\tau_{12}}{\tau_{12}^{\max}}\right)^2 + \left(\frac{\tau_{13}}{\tau_{13}^{\max}}\right)^2 + \left(\frac{\tau_{23}}{\tau_{23}^{\max}}\right)^2 + \left(\frac{\sigma_1}{\sigma_{11,\max}^{T}}\right)^2 \geq 1 \quad (1)$$

$$\mathrm{FI}_2 = \left(\frac{\sigma_1}{\sigma_{11,\max}^{C}}\right)^2 + \left(\frac{\tau_{12}}{\tau_{12}^{\max}}\right)^2 + \left(\frac{\tau_{13}}{\tau_{13}^{\max}}\right)^2 \geq 1 \quad (2)$$

E. Continuous Degradation Rules for Longitudinal Moduli

A strain based degradation rule is proposed for the reduction of E_{ii} (i = 1...3), as described in [45]. The fiber or matrix damage initiates at a user-defined strain $\varepsilon_{ii}^{\text{init}}$, while the stiffness reduction is performed by:

$$E_{ii}^{t+\Delta t} = \begin{cases} E_{ii}^{0}\cdot\left(1 - d_i\cdot\frac{\varepsilon_{ii}^{t+\Delta t} - \varepsilon_{ii}^{\text{init}}}{\Delta\varepsilon_{ii}}\right) & \text{for } \varepsilon_{ii}^{\text{init}} \leq \varepsilon_{ii}^{t+\Delta t} \leq \varepsilon_{ii}^{\text{init}} + \Delta\varepsilon_{ii} \\ E_{ii}^{0}\cdot(1-d_i)\cdot\frac{\varepsilon_{ii}^{\text{init}} + \Delta\varepsilon_{ii}}{\varepsilon_{ii}^{t+\Delta t}} & \text{for } \varepsilon_{ii}^{t+\Delta t} \geq \varepsilon_{ii}^{\text{init}} + \Delta\varepsilon_{ii} \end{cases} \quad (3)$$

where E_{ii}^{0} is the initial modulus of elasticity from Table I in the lamina on-axis system, $\Delta\varepsilon_{ii}$ is a user-defined strain step to ensure a smooth reduction of the properties upon failure, and d_i is the reduction factor. Initial damage strain and corresponding stress $\varepsilon_{ii}^{\text{init}}$ are determined by simulation for FI = 1, with FI = max (FI_1, FI_2). A representation of the moduli of elasticity decrease with the reduction factor is shown in Figure 5.

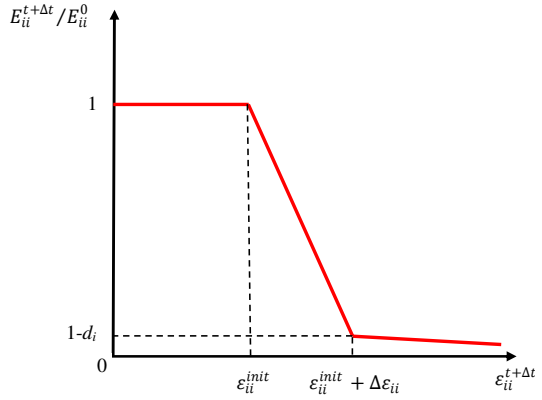

Fig. 5. Stiffness reduction due to damage with a reduction factor d_i.

The reduction parameters for E_{ii} (i =1...3) obtained after several parameter tuning FEA iterations are presented in Table VI.

F. Continuous Degradation Rules for Shear Moduli

In post failure analysis, the in-plane shear moduli G_{ij} are reduced using the maximum shear strains $\gamma_{ij}^{t+\Delta t}$ for FI > 1, according to [45]:

$$G_{ij} = G_{ij}^{0}\left(0.1 + 0.9 \cdot \frac{\gamma_{ij}^{\text{init}}}{\gamma_{ij}^{t+\Delta t}}\right), \quad i \neq j = 1,2,3 \qquad (4)$$

TABLE VI. DEGRADATION PARAMETERS FOR LONGITUDINAL MODULI

Failure mode	d_i	$\Delta\varepsilon_{ii}$
Fiber shear-compression (i = 1)	0.45	0.01
Matrix compression (i = 2,3)	0.57	0.01

G. Poisson Coefficients Reduction

Reduction of Poisson ratios is proposed in order to comply with the elastic stability of the orthotropic materials, as suggested in [19]:

$$\nu_{12} = \nu_{12}^{0} \cdot \sqrt{\frac{E_{11}E_{22}^{0}}{E_{22}E_{11}^{0}}}$$

$$\nu_{13} = \nu_{13}^{0} \cdot \sqrt{\frac{E_{11}E_{33}^{0}}{E_{33}E_{11}^{0}}} \qquad (5)$$

$$\nu_{23} = \nu_{23}^{0} \cdot \sqrt{\frac{E_{22}E_{33}^{0}}{E_{33}E_{22}^{0}}}$$

These conditions are imposed as normal stiffness ratios may vary significantly with degradation. Simultaneously, the material's stress-strain matrix has to be maintained positive, and thus allow the FE solver to perform calculations. Assuming constant product of the major Poisson's ratios before and after reduction (degradation) as $\nu_{ij} \cdot \nu_{ji} = \nu_{ij}^{0} \cdot \nu_{ji}^{0}$ and that $\nu_{ij}/\nu_{ji} = E_{ii}/E_{jj}$, relations (5) are resulting.

H. Simulation Results

The comparison between experimental and numerical results in terms of the geometry parameters (width/hole diameter-*b/D*, and edge distance/hole diameter-*e/D* ratios) effects on damage initiation and progressive failure mechanisms are presented below. Load-displacement curves are shown in Figure 6. From Figure 6 (experimental curves), it can be observed that the friction static force between the aluminum and composite adherents is approximately F_f = 150 N. Considering the adherents clamping force P = 330 N, it is implied that the real friction coefficient should be equal to $\mu = F_f/2P = 150/2 \cdot 330 = 0.227$. This value is quite close to the value used in numerical simulation, μ= 0.235 [43], which suggests that the simulation considered the friction base phenomena with satisfying accuracy. The small difference between the friction coefficient values may be caused by the fact that during the experiments of this study the surfaces of the two adherents were not properly cleaned with the ultrasonic technique as in [43]. However, in the numerical simulation, the constant force indicating friction is not obtained as in the experiment. By comparing the plots, we can see that the increase of geometric parameters has augmented more than twice the force at the limit of linear behavior of the joint (deviation from linearity, point A) and maximum load (point B). At point A on the load-displacement curves, the fiber and matrix compression damage onset around the hole obtained experimentally is evident according to Figure 7. Point A represents the first damage initiation point, denoting the limit load of the joint, and is located at the major deviation of the force-displacement curves from linear behavior. At this point, the compression fiber damage appeared as an indicator of the bearing failure initiation, despite the fact that the fiber-matrix shear damage is also observed in that point. Matrix compression damage is also present at point A but this does not contribute a lot to the joint stiffness loss, as already mentioned, because carbon fibers have the most important role in joint stiffening. The main interests of this study aim towards applications in the aerospace industry, and being on the conservative side, we consider that the limit load is obtained for point A. Beyond this point it is safer to consider that a post failure scenario appears, although the ultimate load is reached in point B. For aerospace joints (whose strength was not proven by limit and ultimate load tests), the approach is very conservative, especially if data are not available or experimental testing is missing, and an additional fitting factor of 1.15 is added to the safety factor of 1.5. So, to cover the uncertainties and to avoid any incidental failures the combined factor of safety becomes 1.725. We prefer to be on the safe side of first-ply failure in our analysis and to consider post failure beyond point A.

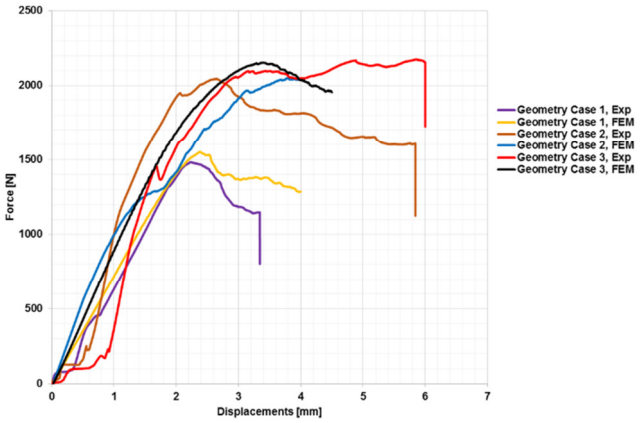

Fig. 6. Load-displacement behavior.

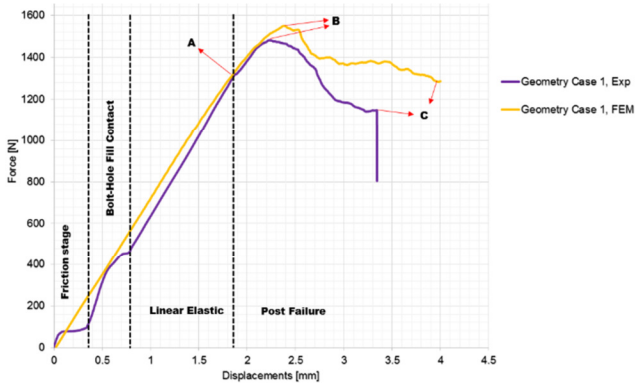

Fig. 7. Force-displacement curves. Geometry Case 1.

As can be seen from Figure 8, in 0° plies, fiber damage is more predominant than matrix damage, while in 90° plies, the two micro level damages have almost the same spread out. In Figures 8-11, the dark blue color represents undamaged elements, while the red color states the E^{0}_{ii} (1-d_i) residual stiffness of the elements. In Figure 8, it can be observed that the damaged layer is located to the top surface of the laminate,

taking into account that the laminate plate was modeled with only one element per each ply in the thickness direction. The first ply failure position could be affected by the bolt tilting in the hole due to the exiting joint clearance and secondary bending effect.

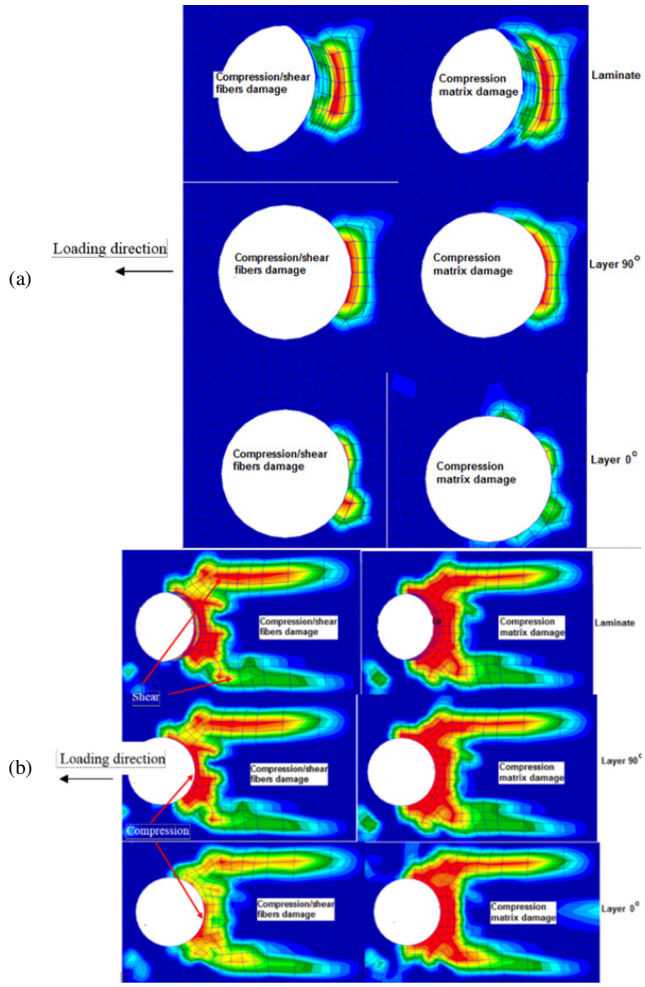

Fig. 8. Bearing damage onset for Case 1: (a) point A, (b) point B.

I. Experimental Results

In Figure 7, point B represents the joint ultimate failure, as explained above. After point A, the damage accumulation determines gradual joint stiffness reduction, and the characteristic curve becomes nonlinear. From point A to point B, the post failure stage is completely developed where the residual stiffness is continuously reduced. On this stage, the fiber compression, matrix compression, and fiber-matrix shear damage are increasing at the bearing plane through the whole thickness of the laminate plate, as it can be seen in Figure 9. Point C (Figure 7) represents the catastrophic final failure of the joint when fiber compression, matrix compression, and fiber-matrix shear damages start, and propagate on approximately +/- 45° from the loading direction. At this point, they are extended to a large portion of the laminate plate on the bearing plane through free edge behind the laminate hole, as it can be easily observed in Figures 7-11. In point B, post failure has been completely developed, and maximum force is reached.

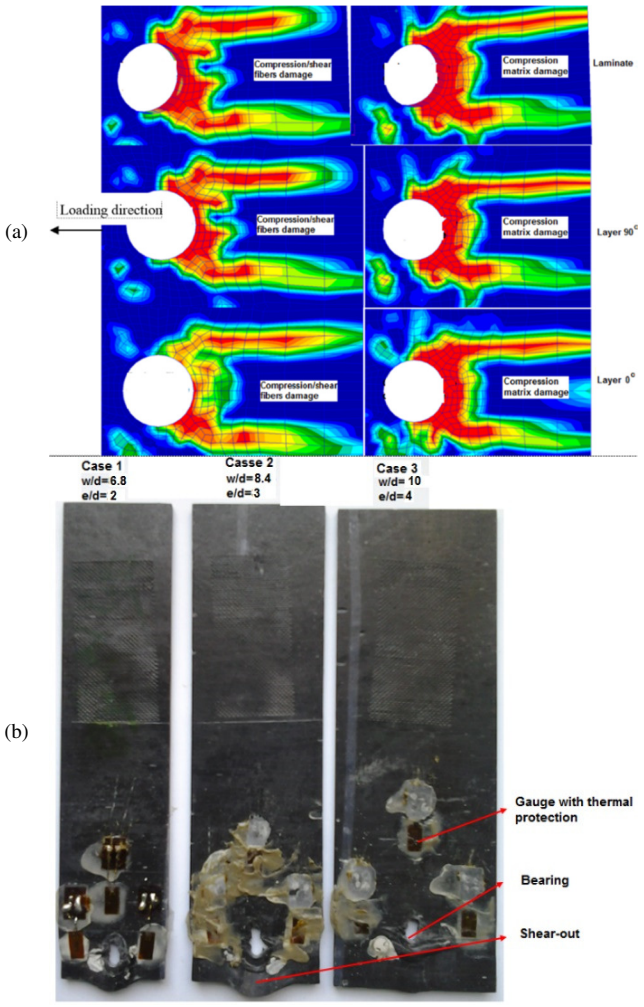

Fig. 9. The geometry influence on the joint failure modes: (a) point C, FEM, Case 1, (b) point C, EXP, all cases.

A summary of the geometry parameter effects on the progressive failure of the metal-composite hybrid joints is presented in Table VII and Figure 12. In Table VII, F_{LL} and $F_{U.L}$ represent the *limit* and *ultimate* forces of the joint to axial quasi-static tensile loading, and are corresponding to the A and B points from the characteristic force-displacement curves discussed above. In Table VII, it is clearly seen that bearing failure mode appears for all values of *b/D* as the joint was designed in accordance with ASTM standard [17] to induce bearing failure. It is also noticed, though, that for *e/D*< 4, shear-out failure mode is present despite the fact that literature research recommends *e/D* < 3 for this type of failure mode. In Figure 12 the influence of the geometric parameter *b/D* on the joint ultimate failure load is illustrated. It can be seen that the curve has an asymptotic value of 2200 N for the ultimate failure load, which denotes that values *b/D* >10 are not recommended because they have no more effects on the joint failure load.

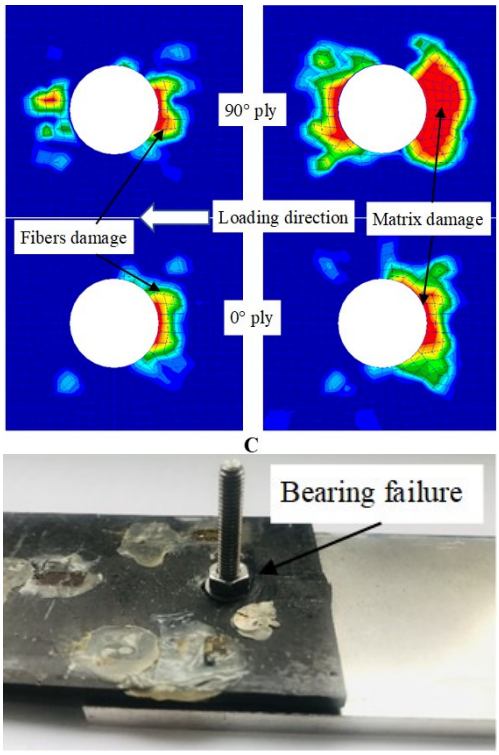

Fig. 10. Catastrophic failure in point C for Case 2: (a) stiffness reduction at catastrophic failure, (b) bearing failure of the composite adherent.

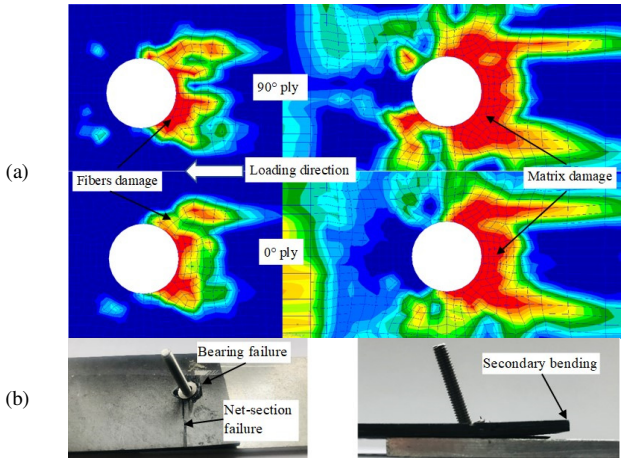

Fig. 11. Catastrophic failure in point C for Case 3: (a) stiffness reduction at catastrofic failure, (b) net section and secondary bending of the composite adherent.

TABLE VII. GEOMETRY EFFECTS ON MACROSCOPIC FAILURE MODES OF THE JOINTS

Geometry	***T*** **[°C]**	**Torque [Nm]**	F_{LL} **[N]**		F_{UL} **[N]**		**Failure mode**
			EXP	FEM	EXP	FEM	
b/D=6.8 *e/D* =2	+50	0.5	1317.43	1376.65	1480.32	1548.94	Bearing/shear-out
b/D=8.4 *e/D*=3			1246.07	1225.65	2044.20	2043.94	Bearing/shear-out
b/D=10 *e/D*=4			1448.37	1500.03	2173.78	2151.84	Bearing

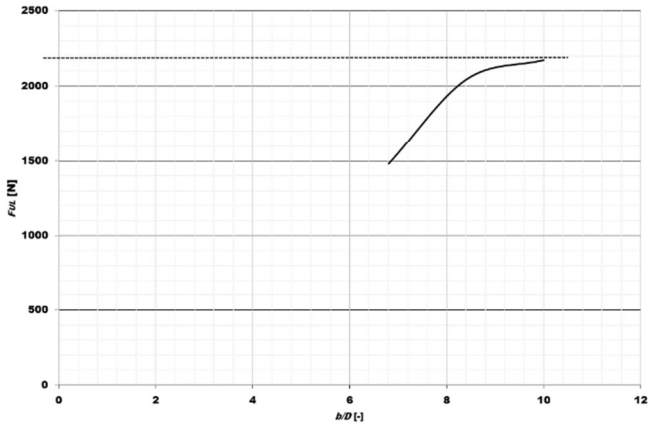

Fig. 12. The influence of *b/D* on joint ultimate failure load.

IV. CONCLUSIONS

In this paper, the effects of the geometry parameters width/hole diameter-*b/D* and edge distance/hole diameter-*e/D* ratios on the stiffness, damage initiation, and progressive failure for single-lap, single-bolt, hybrid metal-composite joints are investigated, using both strain gauge measurements and finite element analysis. The countersunk bolt was chosen, as it determines a complex tridimensional state of stress around the hole, and thus a complex mode of failure in the composite adherent. A 3D FEM model, which incorporates geometrical and friction contact full nonlinearities, was developed in the MSC Patran-Nastran commercial software for predicting the joint stiffness and strength. The PDA material model was implemented with the help of a user-defined subroutine, named User_mat in FORTRAN.

The simulation results were in good agreement with the experiments in terms of load-displacement behavior, surface strain, joint stiffness, and limit and ultimate loads. This denoted that the 3D FEM model, including full nonlinearities and an explicit solver, is quite accurate, and can predict the metal-composite mechanical behavior of the joint in both linear elastic and nonlinear elastic ranges, including bearing, shear-out, and net-section failure modes.

The simulation results were in good agreement with the experiments in terms of surface strains, load-displacement behavior, FPF (First Ply Failure), and ultimate failure loads, This denoted that the 3D FEM model including full nonlinearities and explicit solver are quite accurate, and can predict the metal-composite joint's mechanical behavior on both linear-elastic and nonlinear elastic ranges, including the failure modes as bearing and shear-out. Regarding the geometry effects on the load-displacement curves, it can be seen that loading joint behavior released some interesting features at the beginning stage due to friction between the plates (Figure 6). This friction stage consists of static and dynamic friction. From the graphs, the friction load can be detected and, knowing the clamping force from the torque level, the friction coefficient between the plates can be calculated.

From the numerical and experimental results, it can be deducted that when the geometry parameters (*b/D*, *e/D*)

increase, the ultimate failure loads increase up to an asymptotic value of 2200 N, denoting that the geometry parameters have a limited effect upon the strength of the joint.

All the failure modes appeared in the composite counter part of the joint, and thus the geometry parameters of the joint were selected accordingly.

REFERENCES

[1] Y. Xiao and T. Ishikawa, "Bearing strength and failure behavior of bolted composite joints (part II: modeling and simulation)," *Composites Science and Technology*, vol. 65, no. 7, pp. 1032–1043, Jun. 2005, https://doi.org/10.1016/j.compscitech.2004.12.049.

[2] J. L. Chaboche, "Continuum Damage Mechanics: Part II—Damage Growth, Crack Initiation, and Crack Growth," *Journal of Applied Mechanics*, vol. 55, no. 1, pp. 65–72, Mar. 1988, https://doi.org/10.1115/1.3173662.

[3] F.-K. Chang and K.-Y. Chang, "Post-Failure Analysis of Bolted Composite Joints in Tension or Shear-Out Mode Failure," *Journal of Composite Materials*, vol. 21, no. 9, pp. 809–833, Sep. 1987, https://doi.org/10.1177/002199838702100903.

[4] L. B. Lessard and M. M. Shokrieh, "Two-Dimensional Modeling of Composite Pinned-Joint Failure," *Journal of Composite Materials*, vol. 29, no. 5, pp. 671–697, Mar. 1995, https://doi.org/10.1177/002199839502900507.

[5] C.-L. Hung and F.-K. Chang, "Bearing Failure of Bolted Composite Joints. Part II: Model and Verification," *Journal of Composite Materials*, vol. 30, no. 12, pp. 1359–1400, Aug. 1996, https://doi.org/10.1177/002199839603001204.

[6] S. J. Kim, J. S. Hwang, and J. H. Kim, "Progressive Failure Analysis of Pin-Loaded Laminated Composites Using Penalty Finite Element Method," *AIAA Journal*, vol. 36, no. 1, pp. 75–80, 1998, https://doi.org/10.2514/2.354.

[7] P. P. Camanho and F. L. Matthews, "A Progressive Damage Model for Mechanically Fastened Joints in Composite Laminates," *Journal of Composite Materials*, vol. 33, no. 24, pp. 2248–2280, Dec. 1999, https://doi.org/10.1177/002199839903302402.

[8] M. Q. Le, H. Bainier, D. Neron, C. Ha-Minh, and P. Ladeveze, "On matrix cracking and splits modeling in laminated composites," *Composites Part A: Applied Science and Manufacturing*, vol. 115, pp. 294–301, Dec. 2018, https://doi.org/10.1016/j.compositesa.2018.10.002.

[9] J. Serra, C. Bouvet, B. Castanie, and C. Petiot, "Scaling effect in notched composites: The Discrete Ply Model approach," *Composite Structures*, vol. 148, pp. 127–143, Jul. 2016, https://doi.org/10.1016/j.compstruct.2016.03.062.

[10] L. Adam, C. Bouvet, B. Castanie, A. Daidie, and E. Bonhomme, "Discrete ply model of circular pull-through test of fasteners in laminates," *Composite Structures*, vol. 94, no. 10, pp. 3082–3091, Oct. 2012, https://doi.org/10.1016/j.compstruct.2012.05.008.

[11] P. P. Camanho and M. Lambert, "A design methodology for mechanically fastened joints in laminated composite materials," *Composites Science and Technology*, vol. 66, no. 15, pp. 3004–3020, Dec. 2006, https://doi.org/10.1016/j.compscitech.2006.02.017.

[12] B. Okutan, "The effects of geometric parameters on the failure strength for pin-loaded multi-directional fiber-glass reinforced epoxy laminate," *Composites Part B: Engineering*, vol. 33, no. 8, pp. 567–578, Dec. 2002, https://doi.org/10.1016/S1359-8368(02)00054-9.

[13] K. I. Tserpes, G. Labeas, P. Papanikos, and T. Kermanidis, "Strength prediction of bolted joints in graphite/epoxy composite laminates," *Composites Part B: Engineering*, vol. 33, no. 7, pp. 521–529, Oct. 2002, https://doi.org/10.1016/S1359-8368(02)00033-1.

[14] A. Olmedo and C. Santiuste, "On the prediction of bolted single-lap composite joints," *Composite Structures*, vol. 94, no. 6, pp. 2110–2117, May 2012, https://doi.org/10.1016/j.compstruct.2012.01.016.

[15] Z. Kapidzic, L. Nilsson, and H. Ansell, "Finite element modeling of mechanically fastened composite-aluminum joints in aircraft structures," *Composite Structures*, vol. 109, pp. 198–210, Mar. 2014, https://doi.org/10.1016/j.compstruct.2013.10.056.

[16] M. R. Garnich and V. M. K. Akula, "Review of Degradation Models for Progressive Failure Analysis of Fiber Reinforced Polymer Composites," *Applied Mechanics Reviews*, vol. 62, Dec. 2008, Art. no. 010801, https://doi.org/10.1115/1.3013822.

[17] H. Koerber and P. P. Camanho, "Simulation of progressive damage in bolted composite joints," in *13th European conference on composite materials*, Stockholm, Sweden, Jun. 2008, pp. 1–10.

[18] C. Huhne, A.-K. Zerbst, G. Kuhlmann, C. Steenbock, and R. Rolfes, "Progressive damage analysis of composite bolted joints with liquid shim layers using constant and continuous degradation models," *Composite Structures*, vol. 92, no. 2, pp. 189–200, Jan. 2010, https://doi.org/10.1016/j.compstruct.2009.05.011.

[19] G. Kolks and K. I. Tserpes, "Efficient progressive damage modeling of hybrid composite/titanium bolted joints," *Composites Part A: Applied Science and Manufacturing*, vol. 56, pp. 51–63, Jan. 2014, https://doi.org/10.1016/j.compositesa.2013.09.011.

[20] N. B. Khedher, "Numerical Study of the Thermal Behavior of a Composite Phase Change Material (PCM) Room," *Engineering, Technology & Applied Science Research*, vol. 8, no. 2, pp. 2663–2667, Apr. 2018, https://doi.org/10.48084/etasr.1824.

[21] B. Egan, M. A. McCarthy, R. M. Frizzell, P. J. Gray, and C. T. McCarthy, "Modelling bearing failure in countersunk composite joints under quasi-static loading using 3D explicit finite element analysis," *Composite Structures*, vol. 108, pp. 963–977, Feb. 2014, https://doi.org/10.1016/j.compstruct.2013.10.033.

[22] A. Olmedo, C. Santiuste, and E. Barbero, "An analytical model for the secondary bending prediction in single-lap composite bolted-joints," *Composite Structures*, vol. 111, pp. 354–361, May 2014, https://doi.org/10.1016/j.compstruct.2014.01.015.

[23] O. Allix, N. Bahlouli, C. Cluzel, and L. Perret, "Modelling and identification of temperature-dependent mechanical behaviour of the elementary ply in carbon/epoxy laminates," *Composites Science and Technology*, vol. 56, no. 7, pp. 883–888, Jan. 1996, https://doi.org/10.1016/0266-3538(96)00036-X.

[24] H. S. da Costa Mattos, J. M. L. Reis, L. M. Paim, M. L. da Silva, F. C. Amorim, and V. A. Perrut, "Analysis of a glass fibre reinforced polyurethane composite repair system for corroded pipelines at elevated temperatures," *Composite Structures*, vol. 114, pp. 117–123, Aug. 2014, https://doi.org/10.1016/j.compstruct.2014.04.015.

[25] M.-R. Condruz *et al.*, "A Study on Mechanical Properties of Low-Cost Thermoplastic-Based Materials for Material Extrusion Additive Manufacturing," *Polymers*, vol. 15, no. 14, Jan. 2023, Art. no. 2981, https://doi.org/10.3390/polym15142981.

[26] J. M. L. Reis, F. C. Amorim, A. H. M. F. T. da Silva, and H. S. da Costa Mattos, "Influence of temperature on the behavior of DGEBA (bisphenol A diglycidyl ether) epoxy adhesive," *International Journal of Adhesion and Adhesives*, vol. 58, pp. 88–92, Apr. 2015, https://doi.org/10.1016/j.ijadhadh.2015.01.013.

[27] Z. Jiang, S. Wan, and Z. Wu, "Calculation of energy release rate for adhesive composite/metal joints under mode-I loading considering effect of the non-uniformity," *Composites Part B: Engineering*, vol. 95, pp. 374–385, Jun. 2016, https://doi.org/10.1016/j.compositesb.2016.04.001.

[28] M. Heshmati, R. Haghani, and M. Al-Emrani, "Durability of bonded FRP-to-steel joints: Effects of moisture, de-icing salt solution, temperature and FRP type," *Composites Part B: Engineering*, vol. 119, pp. 153–167, Jun. 2017, https://doi.org/10.1016/j.compositesb.2017.03.049.

[29] Y. Ivanova, "Damage Detection in Free–Free Glass Fiber Fabric Composite Beams by measuring Flexural and Longitudinal Vibrations," *Engineering, Technology & Applied Science Research*, vol. 13, no. 3, pp. 10685–10690, Jun. 2023, https://doi.org/10.48084/etasr.5788.

[30] M. Zahid and S. Al-Zaidee, "Validated Finite Element Modeling of Lightweight Concrete Floors Stiffened and Strengthened with FRP," *Engineering, Technology & Applied Science Research*, vol. 13, no. 4, pp. 11387–11392, Aug. 2023, https://doi.org/10.48084/etasr.6055.

[31] M. Heshmati, R. Haghani, and M. Al-Emrani, "Effects of moisture on the long-term performance of adhesively bonded FRP/steel joints used in bridges," *Composites Part B: Engineering*, vol. 92, pp. 447–462, May 2016, https://doi.org/10.1016/j.compositesb.2016.02.021.

[32] *ASTM D5961-07(2007),Standard Test Method for Bearing Response of Polymer Matrix Composite Laminates*. West Conshohocken, PA, USA: ASTM International, 2007.

[33] M. Chishti, C. H. Wang, R. S. Thomson, and A. C. Orifici, "Experimental investigation of damage progression and strength of countersunk composite joints," *Composite Structures*, vol. 94, no. 3, pp. 865–873, Feb. 2012, https://doi.org/10.1016/j.compstruct.2011.10.011.

[34] *ISO 286-2(2010), Tables of standard tolerance classes and limit deviations for holes and shafts*. Geneva, Switzerland: International Organization for Standardization, 2010.

[35] *ASTM D 3039-02(2002), Standard Test Method for Tensile Properties of Polymer Matrix Composite Materials*. West Conshohocken, PA, USA: ASTM International, 2002.

[36] *ASTM D 3410-07(2007), Standard Test Method for Compressive Properties of Polymer Matrix Composite Materials*. West Conshohocken, PA, USA: ASTM International, 2007.

[37] "ASTM D5379/D5379M-05 - Standard Test Method for Shear Properties of Composite Materials by the V-Notched Beam Method." ASTM, West Conshohocken, PA, USA, 2005.

[38] *Torayca T300, Technical Data Sheet. Report no. CFA-001*. Toray Carbon Fibers America Inc, 2010.

[39] *Derakane Momentum 411-350 Epoxy Venyl Ester Resin, Technical Data Sheet No. 1701 V3 F2*. Ashland Inc, 2010.

[40] R. C. Rice, J. L. Jackson, J. Bakuckas, and S. Thompson, "Metallic Materials Properties Development and Standardization (MMPDS)," Battelle Memorial Inst., Columbus, OH, USA, William J. Hughes Technical Center, Atlantic City, NJ, USA, Office of Aviation, Federal Aviation Administration, Washington, DC, USA, Technical Report PB2003106632, 2003.

[41] C.-D. Coman, "Geometry Effects on Failure Mechanisms of Hybrid Metal- Composite Bolted Joints," *International Journal of Latest Research in Engineering and Technology*, vol. 4, no. 8, pp. 34–51, 2018.

[42] M. A. McCarthy, C. T. McCarthy, V. P. Lawlor, and W. F. Stanley, "Three-dimensional finite element analysis of single-bolt, single-lap composite bolted joints: part I—model development and validation," *Composite Structures*, vol. 71, no. 2, pp. 140–158, Nov. 2005, https://doi.org/10.1016/j.compstruct.2004.09.024.

[43] J. Schon, "Coefficient of friction for aluminum in contact with a carbon fiber epoxy composite," *Tribology International*, vol. 37, no. 5, pp. 395–404, May 2004, https://doi.org/10.1016/j.triboint.2003.11.008.

[44] H. T. Hahn and S. W. Tsai, "Nonlinear Elastic Behavior of Unidirectional Composite Laminae," *Journal of Composite Materials*, vol. 7, no. 1, pp. 102–118, Jan. 1973, https://doi.org/10.1177/002199837300700108.

[45] Z. Hashin, "Failure Criteria for Unidirectional Fiber Composites," *Journal of Applied Mechanics*, vol. 47, no. 2, pp. 329–334, Jun. 1980, https://doi.org/10.1115/1.3153664.